



# Optimizing the binding of the $^*\text{OOH}$ intermediate via axially coordinated Co-N<sub>5</sub> motif for efficient electrocatalytic H<sub>2</sub>O<sub>2</sub> production

Lina Yan<sup>a</sup>, Chao Wang<sup>b</sup>, Yueshuai Wang<sup>c</sup>, Yahui Wang<sup>a</sup>, Zhaozhao Wang<sup>d</sup>, Lirong Zheng<sup>e</sup>, Yue Lu<sup>c,\*</sup>, Ruzhi Wang<sup>b,\*</sup>, Ge Chen<sup>a,\*</sup>

<sup>a</sup> Beijing Key Laboratory for Green Catalysis and Separation, Faculty of Environment and Life, Beijing University of Technology, Beijing 100124, PR China

<sup>b</sup> Institute of Advanced Energy Materials and Devices, Faculty of Materials and Manufacturing, Key Laboratory of Advanced Functional Materials of Education Ministry of China, Beijing University of Technology, Beijing 100124, PR China

<sup>c</sup> Beijing Key Laboratory of Microstructure and Properties of Solids, Faculty of Materials and Manufacturing, Beijing University of Technology, Beijing 100124, PR China

<sup>d</sup> Hebei Technology Innovation Center for Water Pollution Control and Water Ecological Remediation, School of Energy and Environmental Engineering, Hebei University of Engineering, Handan 056038, PR China

<sup>e</sup> Beijing Synchrotron Radiation Facility, Institute of High Energy Physics, Chinese Academy of Sciences, Beijing 100049, PR China

## ARTICLE INFO

### Keywords:

ORR  
Hydrogen peroxide  
Template-sacrificing strategy  
Axial-N  
Active site density

## ABSTRACT

Electrochemical production of hydrogen peroxide (H<sub>2</sub>O<sub>2</sub>) is a sustainable and environmentally benign process. The electrochemical oxygen reduction process (ORR) via a two electron pathway (2e<sup>-</sup> ORR) offers a practical method for on-site H<sub>2</sub>O<sub>2</sub> generation. As an earth-abundant catalyst, the cobalt-nitrogen coordinated systems integrated into the carbon matrix (Co-NC) has caused wide attention for its high activity in 2e<sup>-</sup> ORR. Even though most of the reported Co-NC catalysts have classical planar Co-N<sub>4</sub> coordination, axial coordination engineering has recently emerged as an effective way to control the active sites in the axial direction by using different coordination ligands. The structure-function link between the Co-N configuration of non-planar coordination and 2e<sup>-</sup> ORR activity is, however, not fully understood. An axial-N coordinated Co-N<sub>5</sub> motif embedded in hierarchically porous graphite-3R carbon (Co-N<sub>5</sub>C) was effectively synthesized using a template-sacrificing method. The Co-N<sub>5</sub>C has a high selectivity for 2e<sup>-</sup> ORR and a high H<sub>2</sub>O<sub>2</sub> molar production rate of up to 6.78 mol peroxide/g<sub>catalyst</sub>/h in acidic media, both of which are better than its Co-N<sub>4</sub> counterpart. DFT analyses demonstrate that axial-N ligands regulated the *d*-band center of the Co atom in the Co-N<sub>5</sub>C catalyst, inducing a shift in Δ*G*<sup>\*</sup><sub>OOH</sub> near the Sabatier volcano plot's peak (Δ*G*<sup>\*</sup><sub>OOH</sub> = 4.22 eV). This optimized the binding of the  $^*\text{OOH}$  intermediate and then enhanced the protonation of  $^*\text{OOH}$  to produce H<sub>2</sub>O<sub>2</sub> more efficiently.

## 1. Introduction

H<sub>2</sub>O<sub>2</sub> is a high-value and environmentally friendly oxidizing agent, which has versatile applications in chemical synthesis, environmental remediation, bleaching, semiconductor cleaning, cosmetics, chemical disinfection, etc. The electrochemical synthesis of hydrogen peroxide (H<sub>2</sub>O<sub>2</sub>) via oxygen reduction reaction (ORR) is a green and safe route for on-site and small-scale H<sub>2</sub>O<sub>2</sub> production [1,2]. The ORR can involve multiple electron transfers, which reduce O<sub>2</sub> to produce H<sub>2</sub>O via a four-electron (4e<sup>-</sup>) pathway or H<sub>2</sub>O<sub>2</sub> via a two-electron (2e<sup>-</sup>) pathway [3]. For the 2e<sup>-</sup> ORR, the reaction intermediate,  $^*\text{OOH}$ , is bound by the active sites at optimal energy to facilitate its reduction to H<sub>2</sub>O<sub>2</sub> while preserving the O-O bond in the system. However, O-O bond is

suppressed from being further reduced or dissociated to  $^*\text{O}$  and  $^*\text{OH}$  to form H<sub>2</sub>O in the reaction [4,5].

Since H<sub>2</sub>O<sub>2</sub> degrades readily under alkaline circumstances, considerable work has been put into the efficient production of H<sub>2</sub>O<sub>2</sub> in acidic conditions for downstream uses [5–10]. Unfortunately, the present state-of-the-art electrocatalysts used in acidic environments are limited to precious metal-based alloys, such as Pt-Hg, Pd-Hg, Pt-Au, and Au-Pt-Ni [11–13]. Their broad usage as electrocatalysts is hindered, however, by their high prices, scarcity, and limited selectivity for H<sub>2</sub>O<sub>2</sub> [10]. Consequently, developing active and selective catalysts is crucial, and many efforts have been made to drive the 2e<sup>-</sup> ORR in acidic environments with alternative electrocatalysts based on earth-abundant metals [10,14–18], especially single-atom catalysts [6,7,19,20].

\* Corresponding authors.

E-mail addresses: [luyue@bjut.edu.cn](mailto:luyue@bjut.edu.cn) (Y. Lu), [wrz@bjut.edu.cn](mailto:wrz@bjut.edu.cn) (R. Wang), [chengge@bjut.edu.cn](mailto:chengge@bjut.edu.cn) (G. Chen).

<https://doi.org/10.1016/j.apcatb.2023.123078>

Received 8 May 2023; Received in revised form 22 June 2023; Accepted 6 July 2023

Available online 7 July 2023

0926-3373/© 2023 Elsevier B.V. All rights reserved.

In recent years, the preparation of metal-nitrogen coordinated systems integrated into the carbon matrix (Metal-NC) that are used for energy storage and conversion has exploded. The end-on type of O<sub>2</sub> adsorption on Metal-NC catalysts minimizes the likelihood of O-O bond splitting, hence facilitating the selective production of H<sub>2</sub>O<sub>2</sub> [4]. Several Metal-NC materials (Metal = Mn, Fe, Co, Ni, and Cu) have been investigated experimentally and theoretically for efficient H<sub>2</sub>O<sub>2</sub> generation in acidic conditions. These experiments showed that Co-NC is a remarkable catalyst for producing H<sub>2</sub>O<sub>2</sub> with enhanced selectivity [6,21–23]. Using density functional theory (DFT), theoretical studies determined that the ideal absorption energy for oxygen intermediate (\*OOH) on a metal center is  $4.2 \pm 0.2$  eV for H<sub>2</sub>O<sub>2</sub> generation. The conversion of O<sub>2</sub> to \*OOH regulates the production of H<sub>2</sub>O<sub>2</sub> and is the rate-limiting step due to its high energy absorption [7]. For the Co-N motif, the binding energy for the \*OOH intermediate is near the top of the Sabatier volcano plot, showing a preference for 2e<sup>−</sup> ORR pathway [7]. Prior research has demonstrated that the catalytic performance of M-NC is strongly reliant on the metal's type, coordination sphere, and steric environment. Due to the delicate atomic-level manipulation of the electronic structure, the charge on the Co metal in the Co-NC catalyst is slightly altered, which can further reduce the adsorption of oxygen intermediates on the substrate and increase H<sub>2</sub>O<sub>2</sub> generation [24,25]. Even though the majority of reported Co-NC catalysts possess classical planar Co-N<sub>4</sub> coordination, axial coordination engineering can effectively regulate the active sites in the axial direction using a variety of coordination ligands, thereby endowing the catalysts with novel electronic and chemical properties and achieving a markedly enhanced electrocatalytic performance [26–32].

In this work, a template-sacrificing strategy was adopted to controllably synthesize a Co-N<sub>5</sub>C catalyst containing an axial-N ligand for the effective 2e<sup>−</sup> ORR. In this instance, the carbon support contained an uncommon graphite-3R phase (a rhombohedral phase), a hierarchical porous structure, and a substantial (Brunauer-Emmett-Teller) BET surface area of 801.6 m<sup>2</sup>/g. The catalyst Co-N<sub>5</sub>C demonstrated a high activity (15 mA/cm<sup>2</sup> after 5 h of electrolysis at 0.1 V<sub>RHE</sub>) and selectivity (> 60 % over a wide range of potentials) for 2e<sup>−</sup> ORR in 0.5 M H<sub>2</sub>SO<sub>4</sub>. It also showed a remarkable H<sub>2</sub>O<sub>2</sub> production rate of 6.78 mol H<sub>2</sub>O<sub>2</sub>/g<sub>catalyst</sub>/h at 0.0 V<sub>RHE</sub> in a H-cell, which was much higher than that of Co-N<sub>4</sub>C (0.24 mol H<sub>2</sub>O<sub>2</sub>/g<sub>catalyst</sub>/h) under the same conditions. DFT calculations revealed that the axial-N ligand in Co-N<sub>5</sub>C regulated the *d*-band of the central Co atom and resulted in an increase in free energy change of \*OOH intermediate ( $\Delta G_{*OOH}$ ) to 4.15 eV when compared with Co-N<sub>4</sub> configuration ( $\Delta G_{*OOH} = 3.86$  eV). The  $\Delta G_{*OOH}$  value on Co-N<sub>5</sub> was closer to the peak of the Sabatier volcano plot ( $\Delta G_{*OOH} = 4.22$  eV). As a result, the optimized  $\Delta G_{*OOH}$  on Co-N<sub>5</sub>C promoted the protonation of \*OOH to generate more H<sub>2</sub>O<sub>2</sub>. Besides, the catalyst also demonstrated a low H<sub>2</sub>O<sub>2</sub>RR activity and high durability, suggesting its potential as a highly efficient 2e<sup>−</sup> ORR electrocatalyst.

## 2. Experimental section

### 2.1. Chemicals

All reaction reagents and chemicals were obtained and used in their asreceived form without any further purification. Glycine ( $\geq 99$  %, Shanghai Aladdin Biochemical Technology Co., Ltd.), Cobalt(II) acetate tetrahydrate (99.5 %, Shanghai Aladdin Biochemical Technology Co., Ltd.), MgCl<sub>2</sub>•6 H<sub>2</sub>O (GR,  $\geq 99$  %, Tianjin Fuchen Chemical Reagents Co., Ltd.), Ethanol (GR,  $\geq 99.8$  %, Tianjin Fuchen Chemical Reagents Co., Ltd.), High purity nitrogen (N<sub>2</sub>,  $\geq 99.999$  %, Beijing Qianxijingcheng Gas Co., Ltd.), HCl (hydrochloric acid, AR, Beijing Yili Fine Chemical Co., Ltd.), Nafion solution (5 wt%, Alfa Aesar (China) Chemicals Co., Ltd.), Deionized water was obtained through the water purification system (Milli-Q water) in the lab, H<sub>2</sub>SO<sub>4</sub> (sulfuric acid, GR, Beijing Yili Fine Chemical Co., Ltd.), Ce(SO<sub>4</sub>)<sub>2</sub> (cerous sulfate, 0.01 M, Tianjin Fuchen Chemical Reagents Co., Ltd.), (NH<sub>4</sub>)<sub>2</sub>Fe(SO<sub>4</sub>)<sub>2</sub> (ammonium ferrous

sulfate, 0.01 M, Tianjin Guangfu Fine Chemical Research Institute), Toray carbon paper (TGP-H-60, 19 × 19 cm, Alfa Aesar), Microporous filtration membrane (bore diameter: 0.45 μm, Jinteng).

### 2.2. Catalyst synthesis

Firstly, glycine (0.75 g) was dissolved in deionized water (4 mL) by ultrasound, then hydrated magnesium chloride (1.1 g) was added, and the solution was stirred and heated for 10 min in a water bath (60 °C), 35 mL absolute ethanol was quickly poured into the above solution producing a lot of white complex, centrifuged at 8000 rpm and then dried at 70 °C in the oven. Secondly, 2 g white complex and 0.5 g Co (Ac)<sub>2</sub>•4 H<sub>2</sub>O were pyrolyzed at 800 °C for 2 h under flowing N<sub>2</sub>, obtaining black power (noted Co-MgO/NC). The black power was performed acid etching (concentrated hydrochloric acid, in order to remove MgO and exposed Co particles) in a beaker at room temperature stirring for 12 h, and then washed several times with deionized water, filtered, freeze-dried overnight, noted Co-N<sub>5</sub>C.

### 2.3. Characterization

The X-ray powder diffraction (XRD) patterns were conducted on Bruker D8 Advance X-Ray Diffractometer with Cu Ka. Transmission electron microscopy (TEM) and high resolution TEM (HRTEM) tests were performed on Tecnai F20 microscope at 200 kV. The high angle annular dark field-scanning transmission electron microscopy (HAADF-STEM) and energy dispersive X-ray spectroscopy (EDS) elemental mapping were performed on FEI Titan G2 microscope equipped with a Super-X detector operating at 300 kV. Surface chemical analysis was collected by X-ray photoelectron spectroscopy (XPS) using a Kratos Axis Ultra XPS spectrometer with monochromatized Al-Kα radiation. The nitrogen adsorption-desorption system (Autosorb iQ, Quantachrome Instruments) was used for measuring specific surface areas and pore size distribution under 77 K.

### 2.4. XAS measurements

XAS measurements of Co K-edge were performed at the 1W1B beamline of Beijing Synchrotron Radiation Facility (BSRF). The storage ring was operated at an electron energy of 2.5 GeV with a beam current of 200 mA. Co foil and CoO were used as reference samples and all samples were measured in transmission mode. All samples were pre-treated as discs with diameter of 10 mm and thickness of 1 mm.

The curve fitting and the data analysis were processed using standard procedures with the Athena module implemented in the IFEFFIT software package [33,34]. The k<sup>3</sup>-weighted XAFS spectra were obtained by subtracting the post-edge background from the overall absorption followed by normalization with respect to the edge-jump step. A Hanning window ( $dk=1.0$  Å<sup>−1</sup>) was then used to Fourier transform the k<sup>3</sup>-weighted  $\chi(k)$  data at the Co K-edge into real (R) space.

### 2.5. Electrochemical measurements [35]

The electrochemical properties of the catalyst samples in this work were characterized in a regular three-electrode system with an electrochemical workstation (CHI 760E, CH Instruments, Inc.). A graphite rod was used as the counter electrode and a Ag/AgCl electrode was used as the reference electrode. For the preparation of the working electrode, 3.0 mg of the as-synthesized catalysts was dissolved in 1 mL deionized water, and then mixed with 1.5 mL ethyl alcohol and 0.5 mL of Nafion solution (0.2 wt% Nafion in ethyl alcohol). Next, the mixture was sonicated 20 min below 28 °C. All working electrodes were prepared by depositing the same volume (50 μL) ink onto a carbon paper (TGP-H-60) with a 1 × 1 cm effective area and fully drying. Faradaic efficiency (FE) and production rate of the catalyst samples were proceeded at 0, 0.1, 0.2, 0.3 and 0.4 V<sub>RHE</sub> in O<sub>2</sub>-saturated 0.5 M H<sub>2</sub>SO<sub>4</sub> electrolyte. The yield

of  $\text{H}_2\text{O}_2$  was measured by the method of cerous sulfate determination [36], adopting 0.01 M  $\text{Ce}(\text{SO}_4)_2$  as volumetric solution and  $(\text{NH}_4)_2\text{Fe}(\text{SO}_4)_2$  as indicator. The stability test was carried out continuously for 5 h at 0.1  $V_{\text{RHE}}$  without electrode rotation by using chronoamperometry method.

For the rotating ring disk electrode (RRDE,  $N = 0.37$ ) measurements, a typical three-electrode system were run at room temperature on an electrochemical workstation (CHI 760E, CH Instruments, Inc.) to record the electrochemical response (1600 rpm). A graphite rod was used as a counter electrode and a Ag/AgCl electrode was used as the reference electrode in  $\text{O}_2$ -saturated 0.5 M  $\text{H}_2\text{SO}_4$  electrolyte. The RRDE was polished with 0.5  $\mu\text{m}$  alumina aqueous suspension for 10 min and ultrasonicated in DI water several times. The working electrode was prepared by dropping the catalyst ink on the rotating ring-disk electrode (RRDE, PINE Research Instrumentation, disk area: 0.2475  $\text{cm}^2$ , ring area: 0.1866  $\text{cm}^2$ ) with the catalyst loading of 50  $\mu\text{g}/\text{cm}^2$  and then fully drying. All potentials mentioned in this work were calibrated to the reversible hydrogen electrode (RHE). Cycle voltammetry (CV) was performed between 0.0 and +1.2  $V_{\text{RHE}}$  to electrochemically clean the Pt ring electrode of RRDE until stable CV curve was achieved. The Pt-ring electrode was held at 1.2  $V_{\text{RHE}}$  to assess  $\text{H}_2\text{O}_2$  production at the disk electrode. First,  $\text{N}_2$  gas was input into the electrolyte for 15 min. And then the background current was collected on the disk electrode of RRDE between +1.0 and 0.0  $V_{\text{RHE}}$  at a scan rate of 5 mV/s (rotation speed of 1600 rpm) in  $\text{N}_2$ -saturated 0.5 M  $\text{H}_2\text{SO}_4$ . After that,  $\text{O}_2$  gas was input into the electrolyte for 15 min. Linear sweep voltammetry (LSV) with a scan rate of 5 mV/s and a rotation speed of 1600 rpm was carried out from 0.0 to 1.0  $V_{\text{RHE}}$  in an electrolyte solution under continuous sufficient bubbling with  $\text{O}_2$ .

## 2.6. DFT calculation

DFT calculations were performed using the Vienna Ab initio Simulation Package (VASP) [37]. The exchange-correlation potential was described by using the generalized gradient approximation of Perdew-Burke-Ernzerhof (PBE) [38]. The projector augmented-wave (PAW) method was employed to treat interactions between ion cores and valence electrons [39]. The plane-wave cutoff energy was 500 eV. Given structural models were relaxed until the Hellmann-Feynman forces smaller than  $-0.01$  eV/Å and the change in energy smaller than  $10^{-5}$  eV was attained. During the relaxation, the Brillouin zone was represented by a  $\Gamma$  centered k-point grid of  $2 \times 42 \times 1$ . To avoid the periodic image interaction between the two nearest neighbor unit cells, the vacuum was set to 15 Å in the z-direction. We carried out Spin-polarized calculations including the dipole correlation, the atomic charge density coordinating to the adsorbed species through Bader charge analysis.

## 3. Results and discussion

### 3.1. DFT calculations and ORR mechanism exploration

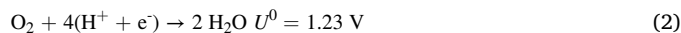
In the past, the Co- $\text{N}_4$  motif has been utilized as the active site of  $2e^-$  ORR for  $\text{H}_2\text{O}_2$  production. Moreover, the modification of the Co- $\text{N}_4$  motif in terms of local oxidation and regulation of N species has been demonstrated to improve its electrochemical performance (details in Table S2). Thus, in order to explore the effect of the axial-N ligand on the activity of the  $2e^-$  ORR, DFT simulations were carried out. Molecular models were developed for both planar Co- $\text{N}_4\text{C}$  and pyramidal Co- $\text{N}_5\text{C}$  to estimate the free energies of the adsorbed intermediates and the kinetic barriers to the reaction.

The atomic configurations of Co- $\text{N}_4\text{C}$  and Co- $\text{N}_5\text{C}$  having well-defined classical planar M- $\text{N}_4$  configuration and an axial-N ligand M- $\text{N}_5$  configuration, respectively, are displayed in Fig. 1a, Figs. S1 and S2.

The  $2e^-$  ORR proceeded in the following order [40]:



The general  $4e^-$  ORR pathway can be depicted as follow [40]:



where \* denotes the active site located on the surface of the catalytic bulk, while  $^*\text{O}$ ,  $^*\text{OH}$ , and  $^*\text{OOH}$  are the adsorbed intermediates.

As shown in Fig. 1b, the partial density of states (PDOS) of Co 3d level in Co- $\text{N}_5\text{C}$  revealed that the axial-N ligand-induced the emergence of new electronic states near the Fermi level. This happened due to the change in the hybridization state of Co in Co- $\text{N}_5\text{C}$ , which promoted rapid electron transfer and the electro-activation of  $\text{O}_2$ . In addition, the PDOS of the central Co atom in Co- $\text{N}_4$  were concentrated within a narrow energy level range, while the PDOS of the central Co atom in Co- $\text{N}_5$  occupied a wider energy level. The center spin up and spin down of Co in Co- $\text{N}_4$  were  $-1.389$  eV and  $-0.618$  eV, respectively, while the center spin up and spin down of Co in Co- $\text{N}_5$  were both  $-1.454$  eV. It should be noted here that the binding between the intermediate  $^*\text{OOH}$  and Co- $\text{N}_4$  was stronger than that of  $^*\text{OOH}$  and Co- $\text{N}_5$  as confirmed by the free energy change,  $\Delta G_{^*\text{OOH}} = -1.06$  eV and  $\Delta G_{^*\text{OOH}} = -0.77$  eV for Co- $\text{N}_4\text{C}$  and Co- $\text{N}_5\text{C}$ , respectively (verified in Fig. 1d). However, this was not conducive to the production of  $\text{H}_2\text{O}_2$ . The  $\Delta G_{^*\text{OOH}}$  of Co- $\text{N}_5$  was close to the equilibrium potential because the axial-N bond significantly reduced the d-band of the central Co atom. Furthermore, the charge density distribution for Co- $\text{N}_4\text{C}$  and Co- $\text{N}_5\text{C}$  was calculated to investigate the electron distribution around the Co atom (Fig. 1c, Fig. S3). DFT calculations suggested that more charge density was accumulated around the N atom in the Co- $\text{N}_5\text{C}$  moiety, implying that the axial-N element captured more electrons from the Co atom [41]. In addition, the Bader charge transfer analysis proved this charge transfer, suggesting the net electron transfer from the Co atom to be 0.67 for the Co- $\text{N}_5\text{C}$  configuration (Fig. S4, Table S1). The free energy diagram of the  $2e^-$  and  $4e^-$  ORR pathway on Co- $\text{N}_4\text{C}$  (left) and Co- $\text{N}_5\text{C}$  (right) at 0  $V_{\text{RHE}}$  is displayed in Fig. 1d. The results showed that Co- $\text{N}_5\text{C}$  was found to be more favorable to the  $2e^-$  pathway than the  $4e^-$  pathway ( $\eta_{\text{H}_2\text{O}_2} = 0.08$  eV,  $\eta_{\text{H}_2\text{O}} = 0.46$  eV), while Co- $\text{N}_4\text{C}$  showed only a small difference for both the processes ( $\eta_{\text{H}_2\text{O}_2} = 0.37$  eV,  $\eta_{\text{H}_2\text{O}} = 0.35$  eV). The reduction of  $^*\text{OOH}$  to  $\text{H}_2\text{O}_2$  was the potential-determining step for the  $2e^-$  pathway, where the Co- $\text{N}_5\text{C}$  required a lower overpotential ( $\eta = 0.08$  eV) than Co- $\text{N}_4\text{C}$  (0.37 eV) for the conversion process, which was confirmed by the volcano plot in Fig. 1f and the electrochemical observations in Fig. 5. In addition, the kinetic energy barriers for the reduction of  $^*\text{OOH}$  to  $\text{H}_2\text{O}_2$  and  $^*\text{O}$  were investigated for Co- $\text{N}_5$  (Fig. 1e, Figs. S5 and S6). The ideal electrocatalyst with high activity and high selectivity toward  $2e^-$  ORR should have a minimum kinetic barrier for the  $\text{H}_2\text{O}_2$  generation. In this view, the  $2e^-$  pathway had a lower kinetic barrier (0.014 eV) than the  $4e^-$  pathway (0.045 eV) for Co- $\text{N}_5$ , as shown in Fig. 1e. This suggested the faster reaction kinetics for  $2e^-$  ORR using Co- $\text{N}_5\text{C}$  as the electrocatalyst. This was again confirmed by the d-band center theory [42], which suggested that the more positive d-center metal atom leads to the strong adsorption of oxygen intermediates on active metal sites. The calculations also revealed that the free energy change of  $^*\text{OOH}$  ( $\Delta G_{^*\text{OOH}} = 4.15$  eV) on Co- $\text{N}_5$  was closer to the peak of  $2e^-$  ORR Sabatier volcano plot ( $\Delta G_{^*\text{OOH}} = 4.22$  eV), as shown in Fig. 1f (details in Table S2). All these results indicated that the Co- $\text{N}_5$  motif was more intrinsically active

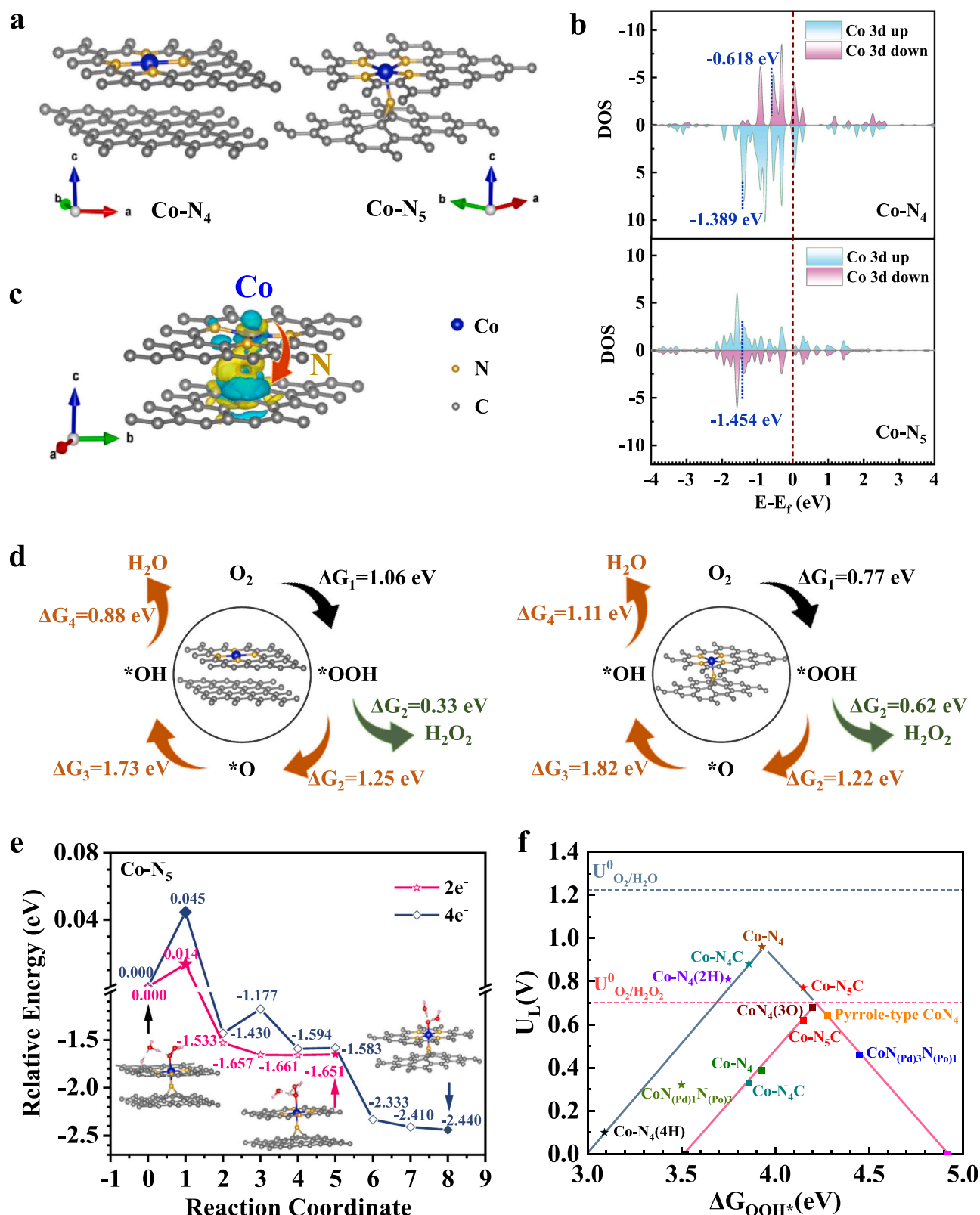


**Fig. 1.** Density Functional Theory calculations. (a) Models of Co-N<sub>4</sub>C and Co-N<sub>5</sub>C; (b) Partial density of states (PDOS) of the Co 3d orbital in Co-N<sub>4</sub>C (up) and Co-N<sub>5</sub>C (down) near the Fermi level ( $E_f$ ), the Fermi level is marked with the dull red dotted line; the blue vertical lines represent the  $d$ -band centers; (c) The charge density difference in the model of Co-N<sub>5</sub>C; (d) Gibbs free energy diagram of the two-electron and four-electron transfer ORR pathway on Co-N<sub>4</sub>C (left) and Co-N<sub>5</sub>C (right), where the labeled absolute values indicate the free energy changes (unit: eV); (e) Kinetic energy barriers to the reduction of \*OOH to \*H<sub>2</sub>O<sub>2</sub> in the two-electron (2e<sup>-</sup>) transfer ORR pathway and \*O in the four-electron (4e<sup>-</sup>) transfer ORR pathway for Co-N<sub>5</sub>; (f) Calculated Sabatier volcano plot for the catalytic 2e<sup>-</sup> ORR to H<sub>2</sub>O<sub>2</sub> obtained from DFT simulations (details in Table S2). The  $U_L$  is plotted as a function of  $\Delta G_{\text{OOH}^*}$ . The pink (square) and blue (star) solid lines represent 2e<sup>-</sup> and 4e<sup>-</sup> theoretical Sabatier volcano, respectively.



toward the  $2e^-$  ORR than the Co-N<sub>4</sub> motif due to the presence of axial-N coordination, which significantly reduced the  $d$ -band center of the Co atom [10]. This ultimately affected the  $\Delta G^*_{OOH}$ , causing a lower kinetic barrier (0.014 eV) for the  $2e^-$  ORR favoring the H<sub>2</sub>O<sub>2</sub> production.

### 3.2. Synthesis and characterization of Co-N<sub>5</sub>C

Encouraged by the results of DFT, an axial-coordinated Co-N<sub>5</sub>C was synthesized using a MgO template-sacrificing strategy [43]. The synthesis of Co-N<sub>5</sub>C and its control sample, Co-N<sub>4</sub>C, is depicted schematically in Fig. 2 (the synthetic procedure is described in detail in the experimental section of Supplementary material).

The powder X-ray diffraction (XRD) patterns in Fig. S7a clearly indicated that Co-MgO/NC (material before acid etching) exhibited graphite-3R (rhombohedral graphite) type structure as confirmed by the standard JCPDS No.26–1079, also the corresponding peaks of MgO and Co phases can also be indexed, which matched very well with their standard JCPDS data 45–0946 and 15–0806, respectively. After the etching process, the XRD pattern of as-obtained Co-N<sub>5</sub>C showed a typical graphite-3R crystal pattern, which matched with JCPDS No. 26–1079, showing the strong reflection at around  $26.6^\circ$  because of the (003) facet of graphite-3R. Moreover, the graphite-3R peaks were clearly confirmed at  $43.45^\circ$ , as shown in Fig. S7c, suggesting the presence of considerable amounts of graphite-3R [44]. Besides, the selected area electron diffraction (SAED) pattern (Fig. S8) further confirmed the existence of the graphite-3R phase [44]. The major presence of the 3 R structure in the work is interesting since the 3 R structure is a semiconductor with tunable band gap and it is less stable than the usually observed graphite-2 H structure [45]. It was observed that nitrogen-doped carbon (NC) synthesized by the pyrolysis of Mg<sup>2+</sup>-glycine complex in the absence of the cobalt species had a relatively low level of graphitization with no traces of MgO phase, as depicted in Fig. S7b. Furthermore, Co-N<sub>4</sub>C prepared using NC as the carbon precursor showed no metallic Co phase. Thus, it can be concluded from the results that the presence of Co species during pyrolysis helps in the formation of graphite carbon, while the co-existence of Co and Mg species during pyrolysis helps in the formation of graphite-3R phase.

The Brunauer-Emmett-Teller (BET) surface area and pore size distribution measurements were carried out through nitrogen adsorption-desorption isotherms. As mentioned in Table S3, Co-N<sub>5</sub>C showed a specific BET surface area of 801.6 m<sup>2</sup>/g, which was slightly larger than that of Co-N<sub>4</sub>C (702.9 m<sup>2</sup>/g). The hysteresis loops of the two samples did not have a typical plateau at high  $P/P^0$  values, as shown in Fig. 3c; and the isotherms belonged to the type IV isotherm with H4 hysteresis loop, indicating that they were mesoporous materials [46]. In addition, under a higher  $P/P^0$  values, the capillary condensation segment of the isotherm for Co-N<sub>5</sub>C was steeper than that of Co-N<sub>4</sub>C, indicating that the distribution of mesoporous in Co-N<sub>5</sub>C was more uniform and the mesoporous pore size was larger. While the results of the pore size distribution, as shown in Fig. S9a, verified the existence of a hysteresis loop with the presence of mesoporosity in the range of 2–30 nm. The corresponding

micropores in the range of 0.4–2 nm were also exhibited by Co-N<sub>5</sub>C, as calculated by the Horvath-Kawazoe (HK) method (Fig. S9b). Moreover, the micropore and mesopore volumes for Co-N<sub>5</sub>C was observed to be larger than Co-N<sub>4</sub>C (Fig. S9, Table S3). Also, the NLDFT method showed that Co-N<sub>5</sub>C is dominant at all aperture sizes based on the distribution of different pore-size structures (Fig. 3d) [47]. This type of hierarchical porous carbon has a micro, meso, and macroporous network that can be tuned to enhance mass transport and catalytic activity [34].

The specific structural details and morphology of Co-N<sub>5</sub>C and Co-N<sub>4</sub>C were investigated by scanning electron microscope (SEM) and transmission electron microscopy (TEM) images. As shown in Fig. S10a–d, Co-N<sub>5</sub>C has flower-like with multiple petals and folds, while Co-N<sub>4</sub>C possesses a flat multi-layer shape. As confirmed by Fig. S10e, f, even after acid washing, both the materials contained residual metallic Co encapsulated in the carbon shell, with Co-N<sub>4</sub>C containing more Co particles than Co-N<sub>5</sub>C. The aberration-adjusted HAADF-STEM image of Co-N<sub>5</sub>C (Fig. 3a, b) indicated the presence of atomically-dispersed Co species in the sample. It should be noted that the as-synthesized Co-N<sub>4</sub>C showed a similar Co dispersion (Fig. S11). The EDS study on Co-N<sub>5</sub>C in the HAADF-STEM mode also showed the uniform distribution of Co, N, C, and O species throughout the carbon matrix (Fig. 3b). To sum up, very few particles were observed on Co-N<sub>5</sub>C sample, and most of Co element exists in the form of Co single atoms. ICP-OES results indicate that the Co content is 1.06 wt% and 0.48 wt% for Co-N<sub>5</sub>C and Co-N<sub>4</sub>C, respectively.

The X-ray absorption fine structure (XAFS) study was carried out at the Co K edge to understand the local atomic and electronic structure of Co-N<sub>5</sub>C and Co-N<sub>4</sub>C. The analysis of the normalized XANES spectra at the Co K-edge of samples (details in Fig. 4a) suggest the average valence state of Co were between 0 valence and +2 valence, and closer to +2 valence (the red arrow) indicating that Co particles were present but in limited numbers for both samples. The Fourier-transformed EXAFS (FT-EXAFS) spectra of Co-N<sub>5</sub>C and Co-N<sub>4</sub>C were very similar, as shown in Fig. 4b. The peak at 1.50 Å for both Co-N<sub>5</sub>C and Co-N<sub>4</sub>C was a contribution of Co-N coordination (Fig. 4b, c, Fig. S12c) [48]. The EXAFS spectra in K-space (Fig. S12a, b) and the related fitting in R-space (Fig. 4c, Fig. S12c) for Co-N<sub>5</sub>C and Co-N<sub>4</sub>C were further plotted to confirm the formation of Co-N bonds. The EXAFS spectra showed that the coordination numbers (CNs) of Co-N in Co-N<sub>5</sub>C and Co-N<sub>4</sub>C were 5.1 and 4.0, respectively, while the mean Co-N bond distances were 1.92 Å and 1.93 Å, respectively. All the EXAFS fitting results of Co-N<sub>5</sub>C and Co-N<sub>4</sub>C were tabulated in Table S4. These results suggested that the Co atom in Co-N<sub>5</sub>C was coordinated with five nitrogen atoms (four square-planar Co-N bonds and one axial Co-N bond), while there were only four square-planar Co-N bonds in Co-N<sub>4</sub>C. The configuration of Co-coordinated with N atoms was also supported by density functional theory (DFT) simulations in Fig. 1a. Also, the second peak at about 2.15 Å corresponding to the Co-Co shell of the two samples, which slightly shifted from the position of the Co-Co scattering peak in Co foil (about 2.17 Å). While the coordination number of the Co-Co shell is only 1.2 for Co-N<sub>5</sub>C (1.3 for Co-N<sub>4</sub>C), confirming a tiny number of remaining Co particles [49–51], which is consistent with the HRTEM result.

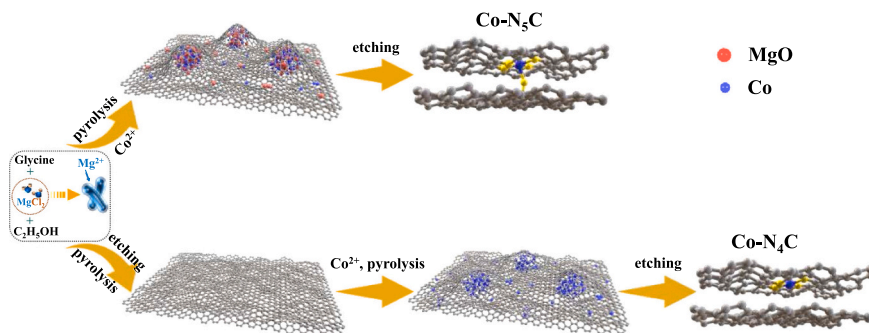


Fig. 2. Schematic diagram of the synthesis of Co-N<sub>5</sub>C and Co-N<sub>4</sub>C.

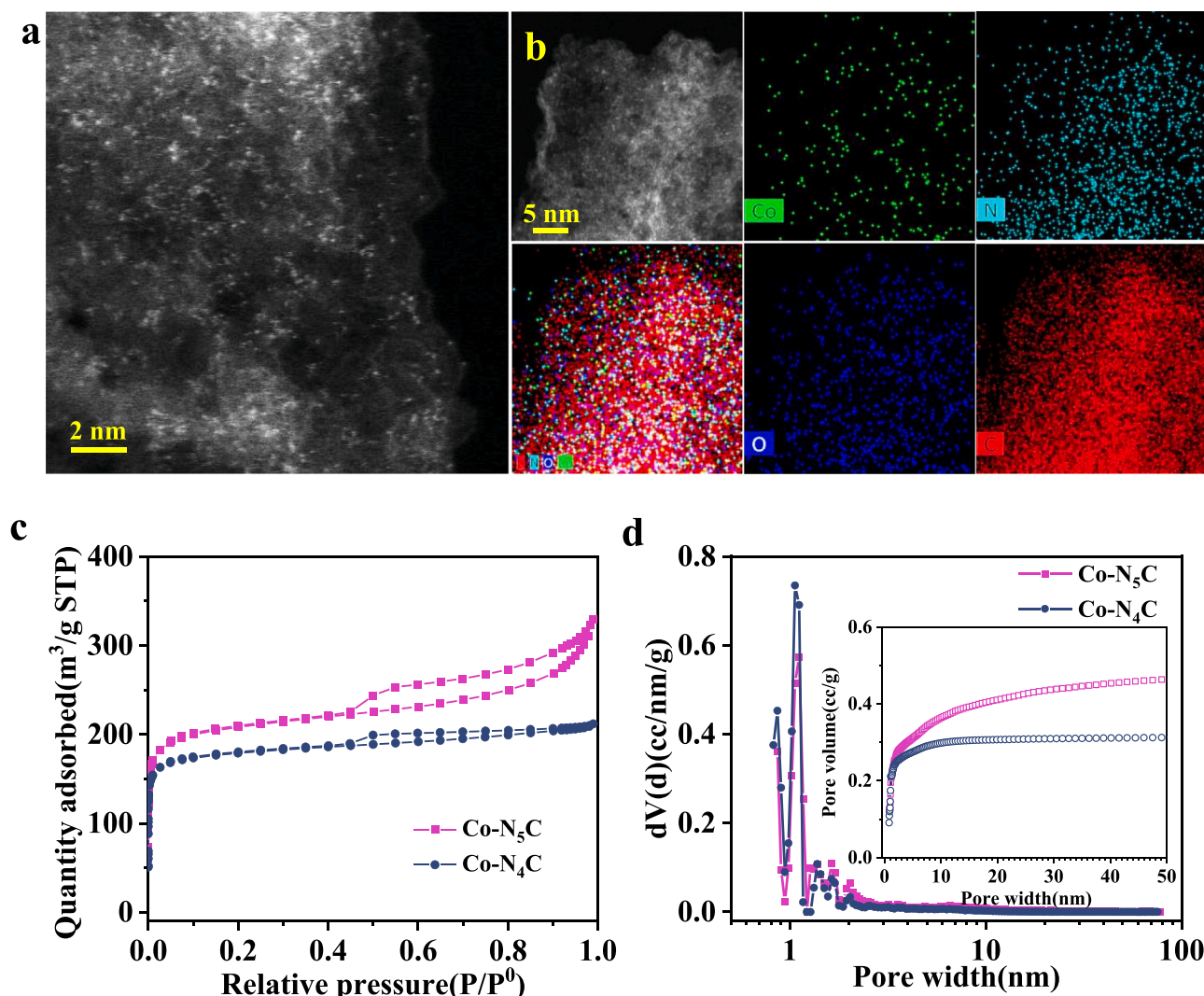


Fig. 3. (a) STEM images of Co-N<sub>5</sub>C, 2 nm; (b) HAADF-STEM image and corresponding EDS maps of Co-N<sub>5</sub>C; (c) N<sub>2</sub> physisorption isotherms of Co-N<sub>5</sub>C and Co-N<sub>4</sub>C catalysts; (d) pore size distribution using NLDFT method; inset shows the pore volumes of Co-N<sub>5</sub>C and Co-N<sub>4</sub>C calculated using NLDFT method.

The surface compositions and electronic states of the samples were characterized using X-ray photoelectron spectroscopy (XPS), as shown in Fig. 4d, e, f and Fig. S13. The wide XPS spectra (Fig. S13a) confirmed the presence of Co, N, and C elements along with the surface-adsorbed O species in all samples. The XPS results revealed the similar C/O content and species for both Co-N<sub>5</sub>C and Co-N<sub>4</sub>C (Table S5, Fig. S13c, d), suggesting the similar C/O chemical environment for both samples. While the Co concentration in Co-N<sub>5</sub>C (0.5 at%) was more than twice as high as that in Co-N<sub>4</sub>C (0.22 at%) (Table S5), which indicated the enrichment of Co species on the surface of Co-N<sub>5</sub>C. The high-resolution XPS spectra of Co 2p 3/2 of Co-N<sub>5</sub>C and Co-N<sub>4</sub>C are shown in Fig. 4d, which indicated the existence of Co<sup>3+</sup> and Co<sup>2+</sup> species in both samples. It should be mentioned here that the ratio of Co<sup>3+</sup>/Co<sup>2+</sup> for Co-N<sub>5</sub>C (about 4.4) was higher than that of Co-N<sub>4</sub>C (about 3.4) (Fig. S13b, Table S6), which agreed well with the aforementioned DFT results (Fig. 1c). It was concluded that the presence of both the states of Co (+3/+2) in Co-N<sub>5</sub>C and Co-N<sub>4</sub>C even after acid washing, which removed unencapsulated metallic Co species, indicated the presence of single metal atom Co-N<sub>x</sub> moieties (Fig. 4e). This results in the maximum exposure of Co-N<sub>x</sub>-based electroactive sites served as the catalytic sites [52]. Thus, in accordance with the earlier research, an analysis of Co 2p XPS spectra revealed that the configuration of Co-N had a significant impact on the electronic structures of Co active centers [26]. The N 1s core-level XPS spectra are presented in Fig. 4e, which indicates the chemical state and amount of N

on the surface of the samples. It has been reported earlier that the pyridine N and pyrrolic N can coordinate with Co to form a Co-N<sub>x</sub> structure, which has a higher ORR activity than sole N-doped carbon [53]. The N 1s spectrum of Co-N<sub>5</sub>C was mainly composed of four peaks, which were assigned to nitrogen atoms with different electronic environments, including pyridinic N (398.4 eV), pyrrolic N/Co-N<sub>x</sub> (399.7 eV), graphitic N (400.9 eV), and N-oxide (403.2 eV). It should be noted here that the stronger coordination affinity of pyrrolic N species enabled them to anchor a single Co atom on its surface [54]. The quantity of pyrrolic N/Co-N<sub>x</sub> moieties in Co-N<sub>5</sub>C was about twice as high as that in Co-N<sub>4</sub>C (17.95 % vs 8.75 %, Fig. 4f), which was similar to the surface Co concentration of the two samples. The Co-N<sub>5</sub> configuration with an axial-N ligand regulated the local electronic structure of the central Co atom [55]. It should be mentioned here that the active site density (SD) of the catalysts, which is one of the important parameters for catalytic reactivity and selectivity, was calculated based on the XPS results and specific surface area data [52] (Fig. 5e). The details of the calculation are provided in Supplementary material “Experimental section”.

### 3.3. ORR performances and experimental investigation

In order to elucidate the electrochemical ORR performance of Co-N<sub>5</sub>C, cyclic voltammetry (CV; Fig. S14) and electrochemical surface area (ECSA) measurements (Fig. S15) were carried out. As shown in Fig. S14,

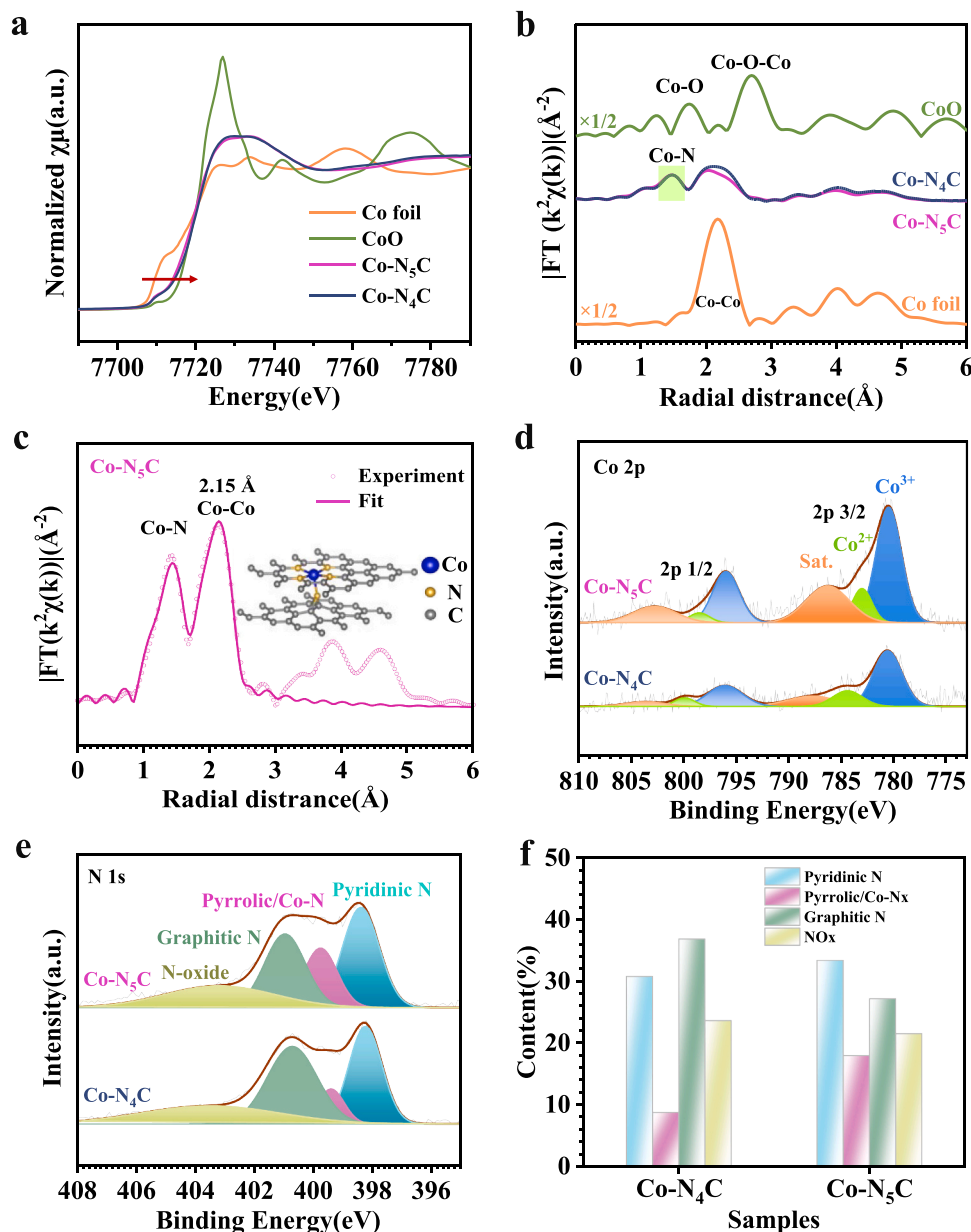


**Fig. 4.** (a) The normalized XANES spectra at the Co K-edge; (b) Fourier-transformed extended X-ray absorption fine structure (FT-EXAFS) spectra at the Co K-edge; (c) Fourier-transformed magnitudes of the Co K-edge EXAFS spectra in R-space for Co-N<sub>5</sub>C with the fitted results; (d) High-resolution Co 2p spectra; (e) High-resolution N 1s spectra of catalysts; (f) High-resolution XPS N 1s spectra of the corresponding relative contents of N species of different catalysts spectra.

Co-N<sub>5</sub>C showed a prominent reduction peak in O<sub>2</sub>-saturated conditions. The double-layer capacitance as a reference of ECSA (Fig. S15) showed that Co-N<sub>5</sub>C with slope = 23.21 mF/cm<sup>2</sup> possessed a higher ECSA than Co-N<sub>4</sub>C (slope = 16.73 mF/cm<sup>2</sup>), indicating that Co-N<sub>5</sub>C had a higher surface area and thus, possessing more active sites [56].

The ORR measurements for the reduction of oxygen to H<sub>2</sub>O<sub>2</sub> were examined using a rotating ring-disk electrode (RRDE) used as the working electrode. The ORR polarization curves were collected on RRDE at 1600 rpm in an O<sub>2</sub>-saturated 0.5 M H<sub>2</sub>SO<sub>4</sub> electrolyte solution. As displayed in Fig. 5a, the Co-N<sub>5</sub>C catalyst showed an onset potential near 0.7 V<sub>RHE</sub>. The H<sub>2</sub>O<sub>2</sub> selectivity in the range of 0.0–0.4 V<sub>RHE</sub> manifested the tendency invariably: Co-N<sub>4</sub>C (about 51–64 %) < Co-N<sub>5</sub>C (60–67 %) (Fig. 5b, Fig. S16a). The selectivity of the electrocatalysts was obtained from the RRDE measurements, which represented the upper limit of electron transfer. In addition, the ORR kinetics was analyzed by the Tafel plot, which is depicted in Fig. 5a inset graph. The excellent ORR activity of Co-N<sub>5</sub>C was verified by the smallest Tafel slope of 186 mV/

dec in comparison to the Co-N<sub>4</sub>C (350 mV/dec), indicating the faster kinetics in the case of the Co-N<sub>5</sub>C sample.

The H<sub>2</sub>O<sub>2</sub> production rate of catalysts was evaluated through an electrolysis experiment in a two-chamber H-cell in an O<sub>2</sub>-saturated 0.5 M H<sub>2</sub>SO<sub>4</sub> with 50 μg/cm<sup>2</sup> catalyst loaded onto a carbon paper cathode. As shown in Fig. 5c, the higher H<sub>2</sub>O<sub>2</sub> faradaic efficiency was observed for Co-N<sub>5</sub>C in comparison to Co-N<sub>4</sub>C in the range of 0.0 V<sub>RHE</sub> (39.9 %) to 0.3 V<sub>RHE</sub> (57.7 %), even in the case of a higher H<sub>2</sub>O<sub>2</sub>RR performance (Fig. S16b). We also test the performance of NC support without Co species, the molar production rate of H<sub>2</sub>O<sub>2</sub> of NC support is very low in 0.5 M H<sub>2</sub>SO<sub>4</sub> electrolyte at each applied potential, as shown in Fig. S16d. It is worth noting here that the Co-N<sub>5</sub>C possessed a high H<sub>2</sub>O<sub>2</sub> molar production rate at every potential, up to 6.78 mol peroxide/g<sub>catalyst</sub>/h at 0.0 V<sub>RHE</sub>, as shown in Fig. 5d. Overall, the electrocatalyst Co-N<sub>5</sub>C had a higher H<sub>2</sub>O<sub>2</sub> molar production rate, faradaic efficiency and slightly higher H<sub>2</sub>O<sub>2</sub>RR performance than Co-N<sub>4</sub>C. However, the faradaic efficiency was lower than the H<sub>2</sub>O<sub>2</sub> selectivity, which was



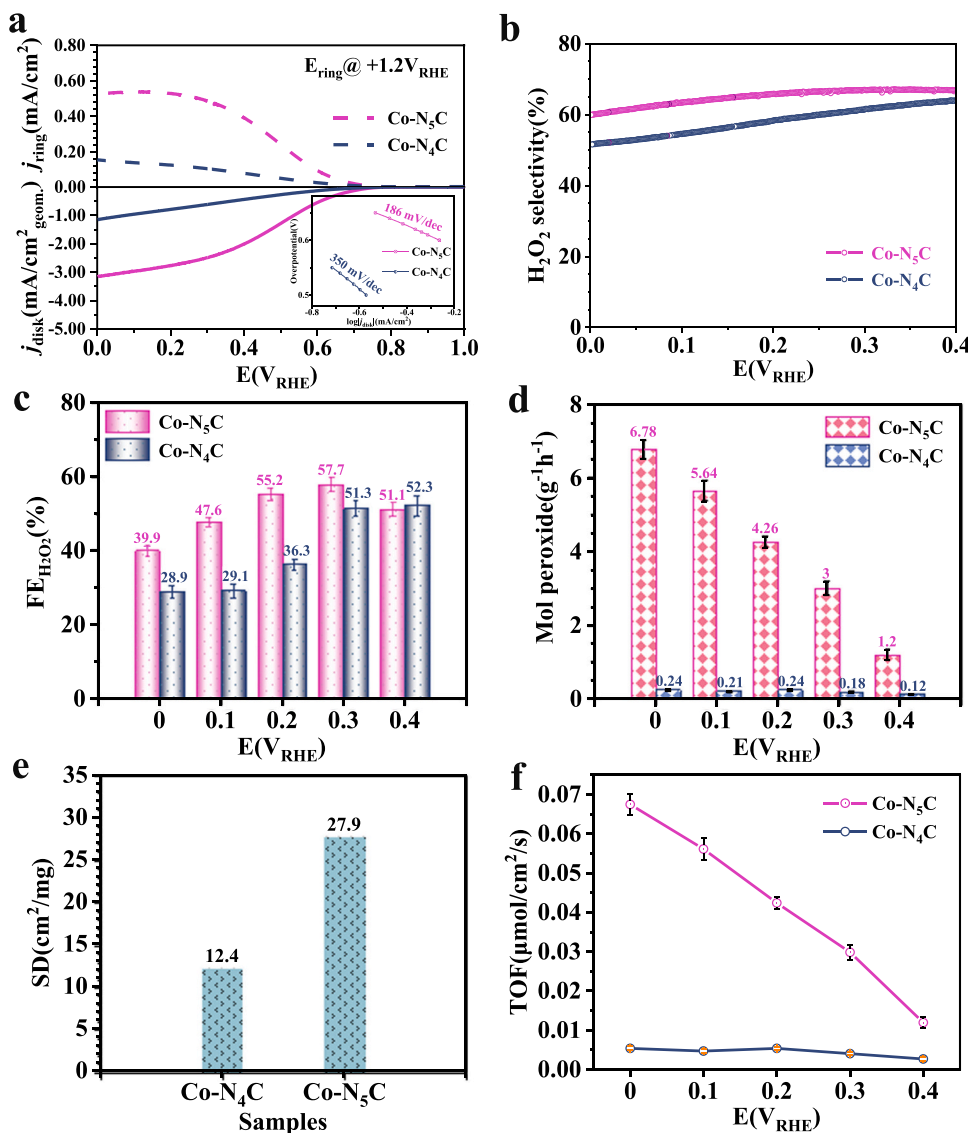


**Fig. 5.** Electrochemical performance of catalysts. (a) ORR performance at 1600 rpm (solid lines) and the simultaneous H<sub>2</sub>O<sub>2</sub> detection current densities at the ring electrode (dashed lines) for catalysts in 0.5 M H<sub>2</sub>SO<sub>4</sub> (the calculated collection efficiency was 0.37), inset shows the Tafel plots; (b) The calculated H<sub>2</sub>O<sub>2</sub> selectivity between 0.0 and 0.4 V<sub>RHE</sub>; (c) Faradaic efficiency (FE, %) of the samples at 0.0, 0.1, 0.2, 0.3, and 0.4 V<sub>RHE</sub> in H-cell; (d) The molar production rate of H<sub>2</sub>O<sub>2</sub> of the samples at 0.0, 0.1, 0.2, 0.3, and 0.4 V<sub>RHE</sub> in H-cell; (e) The SD histogram of the samples; (f) The experimentally-derived H<sub>2</sub>O<sub>2</sub> turnover frequency (TOF) from 0.0 to 0.4 V<sub>RHE</sub>, normalized by Co-N<sub>x</sub> site density (SD).

consistent with the previous work. In addition, the two catalysts remained stable for 5 h in 0.5 M H<sub>2</sub>SO<sub>4</sub> electrolytic solution at 0.1 V<sub>RHE</sub>. The current value of 15.0 mA was obtained in the case of Co-N<sub>5</sub>C, which was much larger than that obtained in the case of Co-N<sub>4</sub>C (Fig. S16c). Moreover, the H<sub>2</sub>O<sub>2</sub> accumulation capacity of Co-N<sub>5</sub>C was tested in the micro-flow-cell at 0.0 V<sub>RHE</sub> during different electrolysis times, as shown in Fig. S16e. The H<sub>2</sub>O<sub>2</sub> yield reached 749 ppm when electrolysis was performed at 0.0 V<sub>RHE</sub> for 4 h Fig. S16f. The remarkable results observed in the case of Co-N<sub>5</sub>C were due to the high site density (SD) and kinetics of the Co-N motif. In addition, the apparent catalytic mass activity (MA) of the catalyst was evaluated on the basis of two descriptors: active SD (aforementioned in the XPS section) and intrinsic catalytic turnover frequency (TOF). The MA was calculated according to the following relation:  $MA = TOF \times SD$  [52,57,58]. The detailed calculation is provided in Supplementary Material Eqs. (8 and 9). The active SD of Co-N<sub>5</sub>C and Co-N<sub>4</sub>C was found to be 27.9 cm<sup>2</sup>/mg and 12.4 cm<sup>2</sup>/mg, respectively. (Fig. 5e, Table S7). Also, the potential-dependent TOF for the two catalysts in the range of 0–0.4 V<sub>RHE</sub> (Fig. 5f) was calculated using Eq. (10) (Table S8), in which Co-N<sub>5</sub>C showed a greater value than Co-N<sub>4</sub>C over the whole potential range. Thus, it was concluded that Co-N<sub>5</sub>C possessed a high active SD and high intrinsic kinetic TOF, which contributed to its superior 2e<sup>-</sup> ORR performance (Tables S9 and S10).

#### 4. Conclusions

In summary, this work demonstrates the template-sacrificing strategy for the synthesis of an axial-coordinated Co-N<sub>5</sub> motif embedded in hierarchical porous graphite-3R carbon. The Co atom in Co-N<sub>5</sub>C was coordinated with five nitrogen atoms in a square-pyramidal configuration. There was a charge transfer between the axial-N ligand and the Co atom, resulting in an optimized local electronic structure. DFT calculations revealed that the free energy change of the oxygen intermediate, \*OOH,  $\Delta G^*_{OOH}$  (4.15 eV) for Co-N<sub>5</sub> configuration was optimized and close to the peak of the volcano plot ( $\Delta G^*_{OOH} = 4.22$  eV), which promoted the protonation of \*OOH to generate more H<sub>2</sub>O<sub>2</sub> than the Co-N<sub>4</sub> configuration. The as-obtained Co-N<sub>5</sub>C catalyst demonstrated highly efficient 2e<sup>-</sup> ORR performance in acidic media, which makes it a promising electrocatalyst for H<sub>2</sub>O<sub>2</sub> production in the future. In addition to the inherent kinetics, the high electrocatalytic activity of Co-N<sub>5</sub>C may be attributed to the high Co-N<sub>5</sub> surface active site density on the hierarchical porous carbon support. Thus, the work provides a facile methodology of non-planar coordination engineering for earth-abundant electrocatalysts for highly efficient H<sub>2</sub>O<sub>2</sub> production in acidic media. Besides, the catalyst also demonstrated a low H<sub>2</sub>O<sub>2</sub>RR activity and high durability, suggesting its potential as a highly efficient 2e<sup>-</sup> ORR electrocatalyst.



## CRediT authorship contribution statement

**Lina Yan:** Conceptualization, Methodology, Investigation, Formal analysis, Data curation, Writing – original draft. **Chao Wang:** Data curation, software. **Yueshuai Wang:** Validation, Data curation. **Yahui Wang:** Data curation. **Zhaozhao Wang:** Data curation. **Lirong Zheng:** Data curation. **Yue Lu:** Data curation. **Ruzhi Wang:** Writing – review & editing. **Ge Chen:** Writing – review & editing, Supervision.

## Declaration of Competing Interest

The authors declare that they have no known competing financial interests or personal relationships that could have appeared to influence the work reported in this paper.

## Data Availability

Data will be made available on request.

## Acknowledgements

This work was supported by the National Natural Science Foundation of China (NSFC 12075015, 12074016 and 12274009), the Beijing Innovation Team Building Program (Grant No. IDHT20190503) and the Beijing Natural Science Foundation (Z210016). The authors thank the 1W1B beamlines radiation equipment of Beijing Synchrotron Radiation Facility.

## Appendix A. Supporting information

Supplementary data associated with this article can be found in the online version at [doi:10.1016/j.apcatb.2023.123078](https://doi.org/10.1016/j.apcatb.2023.123078).

## References

- [1] S.C. Chen, Z.H. Chen, S. Siahrostami, T.R. Kim, D. Nordlund, D. Sokaras, S. Nowak, J.W.F. To, D. Higgins, R. Sinclair, J.K. Nørskov, T.F. Jaramillo, Z.N. Bao, Defective carbon-based materials for the electrochemical synthesis of hydrogen peroxide, *ACS Sustain. Chem. Eng.* 6 (1) (2018) 311–317.
- [2] A. Byeon, J.W. Choi, H.W. Lee, W.C. Yun, W. Zhang, C.-K. Hwang, S.Y. Lee, S. Han, J.M. Kim, J.W. Lee, CO<sub>2</sub>-derived edge-boron-doped hierarchical porous carbon catalysts for highly effective electrochemical H<sub>2</sub>O<sub>2</sub> production, *Appl. Catal. B: Environ.* 329 (2023), 122557.
- [3] Y.Y. Jiang, P.J. Ni, C.X. Chen, Y.Z. Lu, P. Yang, B. Kong, A. Fisher, X. Wang, Selective electrochemical H<sub>2</sub>O<sub>2</sub> production through two-electron oxygen electrochemistry, *Adv. Energy Mater.* 8 (31) (2018) 1801909.
- [4] J.Y. Zhang, H.C. Zhang, M.J. Cheng, Q. Lu, Tailoring the electrochemical production of H<sub>2</sub>O<sub>2</sub>: strategies for the rational design of high-performance electrocatalysts, *Small* 16 (15) (2020) 1902845.
- [5] Z.L. Chen, G.Z. Liu, W.J. Cao, L.X. Yang, L.S. Zhang, S.Q. Zhang, J.P. Zou, R. J. Song, W.H. Fan, S.L. Luo, D.D. Dionysiou, Amorphous low-coordinated cobalt sulphide nanosheet electrode for electrochemically synthesizing hydrogen peroxide in acid media, *Appl. Catal. B: Environ.* 334 (2023), 122825.
- [6] Y.Y. Sun, L. Silvioli, N.R. Sahräie, W. Ju, J.K. Li, A. Zitolo, S. Li, A. Bagger, L. Arnarson, X.L. Wang, T. Moeller, D. Bernsmeier, J. Rossmeisl, F. Jaouen, P. Strasser, Activity-selectivity trends in the electrochemical production of hydrogen peroxide over single-site metal-nitrogen-carbon catalysts, *J. Am. Chem. Soc.* 141 (31) (2019) 12372–12381.
- [7] S. Yang, A.V. Casadevall, L. Arnarson, L. Silvioli, V. Colic, R. Frydendal, J. Rossmeisl, I. Chorkendorff, I.E.L. Stephens, Toward the decentralized electrochemical production of H<sub>2</sub>O<sub>2</sub>: a focus on the catalysis, *ACS Catal.* 8 (5) (2018) 4064–4081.
- [8] J.B. Xi, S. Yang, L. Silvioli, S.F. Cao, P. Liu, Q.Y. Chen, Y.Y. Zhao, H.Y. Sun, J. N. Hansen, J.-P.B. Haraldested, J. Kibsgaard, J. Rossmeisl, S. Bals, S. Wang, I. Chorkendorff, Highly active, selective, and stable Pd single-atom catalyst anchored on N-doped hollow carbon sphere for electrochemical H<sub>2</sub>O<sub>2</sub> synthesis under acidic conditions, *J. Catal.* 393 (2021) 313–323.
- [9] C. Tang, L. Chen, H.J. Li, L.Q. Li, Y. Jiao, Y. Zheng, H.L. Xu, K. Davey, S.Z. Qiao, Tailoring acidic oxygen reduction selectivity on single-atom catalysts via modification of first and second coordination spheres, *J. Am. Chem. Soc.* 143 (20) (2021) 7819–7827.
- [10] L.N. Yan, X. Cheng, Y.S. Wang, Z.Z. Wang, L.R. Zheng, Y. Yan, Y. Lu, S.R. Sun, W. G. Qiu, G. Chen, Exsolved Co<sub>3</sub>O<sub>4</sub> with tunable oxygen vacancies for electrocatalytic H<sub>2</sub>O<sub>2</sub> production, *Mater. Today Energy* 24 (2022), 100931.
- [11] V. Viswanathan, H.A. Hansen, J. Rossmeisl, J.K. Nørskov, Unifying the 2e<sup>-</sup> and 4e<sup>-</sup> reduction of oxygen on metal surfaces, *J. Phys. Chem. Lett.* 3 (20) (2012) 2948–2951.
- [12] R.M. Félix-Navarro, M. Beltrán-Gastélum, E.A. Reynoso-Soto, F. Paraguay-Delgado, G. Alonso-Núñez, J.R. Flores-Hernández, Bimetallic Pt-Au nanoparticles supported on multi-wall carbon nanotubes as electrocatalysts for oxygen reduction, *Renew. Energy* 87 (2016) 31–41.
- [13] Z.K. Zheng, Y.H. Ng, D.W. Wang, R. Amal, Epitaxial growth of Au-Pt-Ni nanorods for direct high selectivity H<sub>2</sub>O<sub>2</sub> production, *Adv. Mater.* 28 (45) (2016) 9949–9955.
- [14] H.Y. Sheng, A.N. Janes, R. Dominic Ross, D. Kaiman, J.Z. Huang, B. Song, J. R. Schmidt, S. Jin, Stable and selective electrosynthesis of hydrogen peroxide and the electro-Fenton process on CoSe<sub>2</sub> polymorph catalysts, *Energy Environ. Sci.* 13 (11) (2020) 4189–4203.
- [15] H.Y. Sheng, E.D. Hermes, X.H. Yang, D.W. Ying, A.N. Janes, W.J. Li, J.R. Schmidt, S. Jin, Electrocatalytic production of H<sub>2</sub>O<sub>2</sub> by selective oxygen reduction using earth-abundant cobalt pyrite (CoS<sub>2</sub>), *ACS Catal.* 9 (9) (2019) 8433–8442.
- [16] J. Liang, Y.Y. Wang, Q. Liu, Y.L. Luo, T.S. Li, H.T. Zhao, S.Y. Lu, F. Zhang, A. M. Asiri, F.G. Liu, D.W. Ma, X.P. Sun, Electrocatalytic hydrogen peroxide production in acidic media enabled by NiS<sub>2</sub> nanosheets, *J. Mater. Chem. A* 9 (10) (2021) 6117–6122.
- [17] F.P. Kong, R.T. Si, N. Chen, Q. Wang, J.J. Li, G.P. Yin, M. Gu, J.J. Wang, L.M. Liu, X.L. Sun, Origin of hetero-nuclear Au-Co dual atoms for efficient acidic oxygen reduction, *Appl. Catal. B: Environ.* 301 (2022), 120782.
- [18] X. Huang, W. Zhang, W. Liu, J.J. Zhang, M. Song, C. Zhang, J. Zhang, D.L. Wang, Nb<sub>2</sub>CT<sub>x</sub> MXenes functionalized Co-NC enhancing electrochemical H<sub>2</sub>O<sub>2</sub> production for organics degradation, *Appl. Catal. B: Environ.* 317 (2022), 121737.
- [19] Y.H. Han, Y.G. Wang, W.X. Chen, R.R. Xu, L.R. Zheng, J. Zhang, J. Luo, R.A. Shen, Y.Q. Zhu, W.C. Cheong, C. Chen, Q. Peng, D.S. Wang, Y.D. Li, Hollow N-doped carbon spheres with isolated cobalt single atomic sites: superior electrocatalysts for oxygen reduction, *J. Am. Chem. Soc.* 139 (48) (2017) 17269–17272.
- [20] K. Kumar, L. Dubau, M. Meermoux, J.K. Li, A. Zitolo, J. Nelayah, F. Jaouen, F. Maillard, On the influence of oxygen on the degradation of Fe-N-C catalysts, *Angew. Chem. Int. Ed.* 59 (8) (2020) 3235–3243.
- [21] J.J. Gao, H.B. Yang, X. Huang, S.-F. Hung, W.Z. Cai, C.M. Jia, S. Miao, H.M. Chen, X.F. Yang, Y.Q. Huang, T. Zhang, B. Liu, Enabling direct H<sub>2</sub>O<sub>2</sub> production in acidic media through rational design of transition metal single atom catalyst, *Chem* 6 (3) (2020) 658–674.
- [22] W. Liu, C. Zhang, J.J. Zhang, X. Huang, M. Song, J.W. Li, F. He, H.P. Yang, J. Zhang, D.L. Wang, Tuning the atomic configuration of Co-N-C electrocatalyst enables highly-selective H<sub>2</sub>O<sub>2</sub> production in acidic media, *Appl. Catal. B: Environ.* 310 (2022), 121312.
- [23] Y.H. Wu, Y.F. Ding, X. Han, B.B. Li, Y.F. Wang, S.Y. Dong, Q.L. Li, S.X. Dou, J. Y. Sun, J.H. Sun, Modulating coordination environment of Fe single atoms for high-efficiency all-pH-tolerated H<sub>2</sub>O<sub>2</sub> electrochemical production, *Appl. Catal. B: Environ.* 315 (2022), 121578.
- [24] H.J. Shen, N.X. Qiu, L. Yang, X.Y. Guo, K. Zhang, T.J. Thomas, S.Y. Du, Q.F. Zheng, J.P. Attfield, Y. Zhu, M.H. Yang, Boosting oxygen reduction for high-efficiency H<sub>2</sub>O<sub>2</sub> electrosynthesis on oxygen-coordinated Co-N-C catalysts, *Small* 18 (17) (2022) 2200730.
- [25] J.J. Liu, Z.X. Wei, Z.C. Gong, M.M. Yan, Y.F. Hu, S.L. Zhao, G.L. Ye, H.L. Fei, Single-atom CoN<sub>4</sub> sites with elongated bonding induced by phosphorus doping for efficient H<sub>2</sub>O<sub>2</sub> electrosynthesis, *Appl. Catal. B: Environ.* 324 (2023), 122267.
- [26] U.I. Kramm, J. Herranz, N. Larouche, T.M. Arruda, M. Lefèvre, F. Jaouen, P. Bogdanoff, S. Fiechter, I.A. Wurmbach, S. Mukerjee, J.-P. Dodelet, Structure of the catalytic sites in Fe/N-C-catalysts for O<sub>2</sub>-reduction in PEM fuel cells, *Phys. Chem. Chem. Phys.* 14 (33) (2012) 11673–11688.
- [27] R.G. Cao, R. Thapa, H.J. Kim, X.D. Xu, M.G. Kim, Q. Li, N. Park, M. Liu, J. Cho, Promotion of oxygen reduction by a bio-inspired tethered iron phthalocyanine carbon nanotube-based catalyst, *Nat. Commun.* 4 (2013) 2076.
- [28] X.Y. Zhou, C. Xu, P.P. Guo, W.L. Sun, P.J. Wei, J.G. Liu, Axial ligand coordination tuning of the electrocatalytic activity of iron porphyrin electrografted onto carbon nanotubes for the oxygen reduction reaction, *Chem. -Eur. J.* 27 (38) (2021) 9898–9904.
- [29] Y.R. Liu, X.J. Liu, Z.H. Lv, R. Liu, L.H. Li, J.M. Wang, W.X. Yang, X. Jiang, X. Feng, B. Wang, Tuning the spin state of the iron center by bridge-bonded Fe-O-Ti ligands for enhanced oxygen reduction, *Angew. Chem. Int. Ed.* 61 (21) (2022), e202117617.
- [30] X.J. Liu, Y.R. Liu, W.X. Yang, X. Feng, B. Wang, Controlled modification of axial coordination for transition-metal single-atom electrocatalyst, *Chem. -Eur. J.* 28 (59) (2022), e202201471.
- [31] W.J. Zhang, J.W. Choi, S. Kim, T.T. Le, S. Nandy, C.-K. Hwang, S.Y. Paek, A. Byeon, K.H. Chae, S.Y. Lee, S.H. Kim, H. Song, J. Kim, J.H. Oh, J.W. Lee, S.S. Han, J. M. Kim, Penta nitrogen coordinated cobalt single atom catalysts with oxygenated carbon black for electrochemical H<sub>2</sub>O<sub>2</sub> production, *Appl. Catal. B: Environ.* 331 (2023), 122712.
- [32] Q.L. Zhao, Y. Wang, W.-H. Lai, F. Xiao, Y.X. Lyu, C.Z. Liao, M.H. Shao, Approaching a high-rate and sustainable production of hydrogen peroxide: oxygen reduction on Co-N-C single-atom electrocatalysts in simulated seawater, *Energy Environ. Sci.* 14 (10) (2021) 5444–5456.
- [33] X. Cheng, Y. Lu, L.R. Zheng, Y.T. Cui, M. Niibe, T. Tokushima, H.Y. Li, Y.F. Zhang, G. Chen, S.R. Sun, J.J. Zhang, Charge redistribution within platinum-nitrogen coordination structure to boost hydrogen evolution, *Nano Energy* 73 (2020), 104739.
- [34] S. Siahrostami, S.J. Villegas, A.H.B. Mostaghimi, S. Back, A.B. Farimani, H. T. Wang, K.A. Persson, J. Montoya, A review on challenges and successes in

- atomic-scale design of catalysts for electrochemical synthesis of hydrogen peroxide, *ACS Catal.* 10 (14) (2020) 7495–7511.
- [35] E. Jung, H. Shin, B. Lee, V. Efremov, S. Lee, H.S. Lee, J. Kim, W.H. Antink, S. Park, K. Lee, S. Cho, J.S. Yoo, Y. Sung, T. Hyeon, Atomic-level tuning of Co-N-C catalyst for high-performance electrochemical H<sub>2</sub>O<sub>2</sub> production, *Nat. Mater.* 19 (4) (2020) 436–442.
- [36] S.M. Yu, X. Cheng, Y.S. Wang, B. Xiao, Y.R. Xing, J. Ren, Y. Lu, H.Y. Li, C. Q. Zhuang, G. Chen, High activity and selectivity of single palladium atom for oxygen hydrogenation to H<sub>2</sub>O<sub>2</sub>, *Nat. Commun.* 13 (2022) 4737.
- [37] G. Kresse, J. Furthmüller, Efficient iterative schemes for ab initio total-energy calculations using a plane-wave basis set, *Phys. Rev. B* 54 (16) (1996) 11169–11186.
- [38] J.P. Perdew, K. Burke, M. Ernzerhof, Generalized gradient approximation made simple, *Phys. Rev. Lett.* 77 (18) (1996) 3865–3868.
- [39] P.E. Blochl, Projector augmented-wave method, *Phys. Rev. B* 50 (24) (1994) 17953–17979.
- [40] S.Y. Chen, T. Luo, X.Q. Li, K.J. Chen, J.W. Fu, K. Liu, C. Cai, Q.Y. Wang, H.M. Li, Y. Chen, C. Ma, L. Zhu, Y.R. Lu, T.S. Chan, M.S. Zhu, Identification of the highly active Co-N<sub>4</sub> coordination motif for selective oxygen reduction to hydrogen peroxide, *J. Am. Chem. Soc.* 144 (32) (2022) 14505–14516.
- [41] W.L. Zhang, E.J. Meeus, L. Wang, L.H. Zhang, S.C. Yang, B.D. Bruin, J.N.H. Reek, F. S. Yu, Boosting electrochemical oxygen reduction performance of iron phthalocyanine through axial coordination sphere interaction, *ChemSusChem* 15 (3) (2022), e202102379.
- [42] B. Hammer, J.K. Nørskov, Theoretical surface science and catalysis-calculations and concepts, *Adv. Catal.* 45 (2000) 71–129.
- [43] S. Liu, Y.C. Zhang, B.H. Ge, F.C. Zheng, N. Zhang, M. Zuo, Y. Yang, Q.W. Chen, Constructing graphitic-nitrogen-bonded pentagons in interlayer-expanded graphene matrix toward carbon-based electrocatalysts for acidic oxygen reduction reaction, *Adv. Mater.* 33 (42) (2021) 2103133.
- [44] T. Ogawara, J.J. Akai, Graphite-3R in a fault fracture zone associated with black jadeite from Kanayamadani, Itoigawa, central Japan, *JMPS* 109 (3) (2014) 125–137.
- [45] M.S. Seehra, U.K. Geddam, D. Schwegler-Berry, A.B. Stefaniak, Detection and quantification of 2H and 3R phases in commercial graphene-based materials, *Carbon* 95 (2015) 818–823.
- [46] K.S.W. Sing, R.T. Williams, Physisorption hysteresis loops and the characterization of nanoporous materials, *Adsorpt. Sci. Technol.* 22 (10) (2004) 773–782.
- [47] S. Storck, H. Bretinger, W.F. Maier, Characterization of micro- and mesoporous solids by physisorption methods and pore-size analysis, *Appl. Catal. A Gen.* 174 (1998) 137–146.
- [48] Y.J. Sa, S.O. Park, G.Y. Jung, T.J. Shin, H.Y. Jeong, S.K. Kwak, S.H. Joo, Heterogeneous Co-N/C electrocatalysts with controlled cobalt site densities for the hydrogen evolution reaction: structure-activity correlations and kinetic insights, *ACS Catal.* 9 (2019) 83–97.
- [49] Q.Q. Cheng, S.B. Han, K. Mao, C. Chen, L.J. Yang, Z.Q. Zou, M. Gu, Z. Hu, H. Yang, Co nanoparticle embedded in atomically-dispersed Co-N-C nanofibers for oxygen reduction with high activity and remarkable durability, *Nano Energy* 52 (2018) 485–493.
- [50] Y.J. Chen, S.F. Ji, Y.G. Wang, J.C. Dong, W.X. Chen, Z. Li, R.G. Shen, L.R. Zheng, Z. B. Zhuang, D.S. Wang, Y.D. Li, Isolated single iron atoms anchored on N-doped porous carbon as an efficient electrocatalyst for the oxygen reduction reaction, *Angew. Chem. Int. Ed.* 56 (2017) 6937–6941.
- [51] Z. Wang, X.Y. Jin, R.J. Xu, Z.B. Yang, S.D. Ma, T. Yan, C. Zhu, J. Fang, Y.P. Liu, S.-J. Hwang, Z.J. Pan, H.J. Fan, Cooperation between dual metal atoms and nanoclusters enhances activity and stability for oxygen reduction and evolution, *ACS Nano* 17 (9) (2023) 8622–8633.
- [52] C.X. Li, W. Ju, S. Vijay, J. Timoshenko, K.W. Mou, D.A. Cullen, J. Yang, X.L. Wang, P. Pachfule, S. Brückner, H.S. Jeon, F.T. Haase, S.C. Tsang, C. Rettenmaier, K. Chan, B.R. Cuenya, A. Thomas, P. Strasser, Covalent organic framework (COF) derived Ni-N-C catalysts for electrochemical CO<sub>2</sub> reduction: unraveling fundamental kinetic and structural parameters of the active sites, *Angew. Chem. Int. Ed.* 61 (2022), e202114707.
- [53] G. Wu, P. Zelenay, Nanostructured nonprecious metal catalysts for oxygen reduction reaction, *Acc. Chem. Res.* 46 (8) (2013) 1878–1889.
- [54] Y. Pan, R. Lin, Y.J. Chen, S.J. Liu, W. Zhu, X. Cao, W.X. Chen, K.L. Wu, W.-C. Cheong, Y. Wang, L.R. Zheng, J. Luo, Y. Lin, Y.Q. Liu, C.G. Liu, J. Li, Q. Lu, X. Chen, D.S. Wang, Q. Peng, C. Chen, Y.D. Li, Design of single-atom Co-N<sub>5</sub> catalytic site: a robust electrocatalyst for CO<sub>2</sub> reduction with nearly 100% CO selectivity and remarkable stability, *J. Am. Chem. Soc.* 140 (2018) 4218–4221.
- [55] F. He, Y.J. Zhao, X.X. Yang, S.X. Zheng, B. Yang, Z.J. Li, Y.B. Kuang, Q.H. Zhang, L. C. Lei, M. Qiu, L.M. Dai, Y. Hou, Metal-organic frameworks with assembled bifunctional microreactor for charge modulation and strain generation toward enhanced oxygen electrocatalysis, *ACS Nano* 16 (6) (2022) 9523–9534.
- [56] L.T. Menisa, P. Cheng, C. Long, X.Y. Qiu, Y.L. Zheng, J.Y. Han, Y. Zhang, Y. Gao, Z. Y. Tang, Insight into atomically dispersed porous M-N-C single-site catalysts for electrochemical CO<sub>2</sub> reduction, *Nanoscale* 12 (2020) 16617–16626.
- [57] N. Leonard, W. Ju, I. Sinev, J.L. Steinberg, F. Luo, A.S. Varela, B.R. Cuenya, P. Strasser, The chemical identity, state and structure of catalytically active centers during the electrochemical CO<sub>2</sub> reduction on porous Fe-nitrogen-carbon (Fe-N-C) materials, *Chem. Sci.* 9 (2018) 5064–5073.
- [58] N. Leonard, S. Wagner, F. Luo, J.L. Steinberg, W. Ju, N. Weidler, H. Wang, U. I. Kramm, P. Strasser, Deconvolution of utilization, site density, and turnover frequency of Fe nitrogen carbon oxygen reduction reaction catalysts prepared with secondary N-precursors, *ACS Catal.* 8 (3) (2018) 1640–1647.